Eur. Phys. J. B **11**, 345–360 (1999)

THE EUROPEAN
PHYSICAL JOURNAL B
EDP Sciences

Multi-affinity and multi-fractality in systems of chaotic elements with long-wave forcing

H. Nakao[a] and Y. Kuramoto

Department of Physics, Graduate School of Sciences, Kyoto University, Kyoto 606-8502, Japan

Received 16 November 1998

Abstract. Multi-scaling properties in quasi-continuous arrays of chaotic maps driven by long-wave random force are studied. The spatial pattern of the amplitude $X(x,t)$ is characterized by multi-affinity, while the field defined by its coarse-grained spatial derivative $Y(x,t) := |(X(x+\delta,t) - X(x,t))/\delta|$ exhibits multi-fractality. The strong behavioral similarity of the X- and Y-fields respectively to the velocity and energy dissipation fields in fully-developed fluid turbulence is remarkable, still our system is unique in that the scaling exponents are parameter-dependent and exhibit nontrivial q-phase transitions. A theory based on a random multiplicative process is developed to explain the multi-affinity of the X-field, and some attempts are made towards the understanding of the multi-fractality of the Y-field.

PACS. 05.45.-a Nonlinear dynamics and nonlinear dynamical systems – 47.53.+n Fractals

1 Introduction

The notions of *multi-affinity* and *multi-fractality*, which are the two specific forms of *multi-scaling*, are useful in characterizing singular measures observed in a wide class of complex dissipative systems far from equilibrium. For example, the velocity field of fully-developed turbulence [1,2] and rough interfaces in fractal surface growth [3–6] exhibit multi-affinity, while the energy dissipation rate in fully-developed turbulence [2,7] and the invariant measures of chaotic attractors in dynamical systems [8–10] are known to be multi-fractal.

In our previous papers, we studied large assemblies of simple dynamical units (*e.g.*, limit-cycle oscillators and chaotic maps) with non-local coupling [11,12], or without coupling but subjected to a randomly fluctuating long-wave external field [13]. A remarkable feature shared commonly by these systems is amplitude fluctuations characterized by power-law initial decay of spatial correlation with a parameter-dependent exponent. More generally, the qth order structure function $\langle h(l)^q \rangle$ associated with the amplitude increments $h(x,l) := |X(x+\frac{l}{2}) - X(x-\frac{l}{2})|$ behaves as $l^{\zeta(q)}$, where the exponent $\zeta(q)$, aside from its parameter dependence, has a nonlinear dependence on q. The latter property is called *multi-affinity*. It was also found that the field Y defined by a coarse-grained spatial derivative of X through $Y(x) := |(X(x+\delta) - X(x))/\delta|$ exhibits *multi-fractality*. By this we mean that the qth moment of the measure $m(x,l) := \int_l Y(x')\mathrm{d}x'$ over the interval l behaves as $l^{\tau(q)}$ with the exponent $\tau(q)$ depending nonlinearly on q.

It is remarkable that this type of anomalous turbulent state can arise in various systems under broad conditions [11–15]. Given a distributed system of active dynamical elements, the only necessary condition for such behavior to be observed is that the individual elements are subjected to a long-wave fluctuating field which may be either of external origin or the one generated internally through some long-range interaction. Under such conditions, a small group of local elements may occasionally lose synchrony with the driving field, which also implies the loss of mutual synchrony within the group, thus giving rise to bursting fluctuations and spatial intermittency. Recent discovery of the same type of turbulence in a three-component reaction-diffusion system [15] provided further evidence for the ubiquity of the phenomenon.

In the present paper, we will focus on the multi-scaling properties of quasi-continuous arrays of chaotic maps, with particular attention to their similarity to fully-developed fluid turbulence. In particular, we investigate the probability distribution functions (PDF) for two kinds of measure, $h(l)$ and $m(l)$, with which a complete specification of the multi-scaling properties can be made. We also attempted a 'microscopic' explanation for the observed shape of the PDFs.

Our paper is organized as follows. In Section 2, we introduce a simple class of models and illustrate their anomalous intermittent behavior. In Section 3, some definitions are introduced and more extensive numerical results on multi-affine and multi-fractal properties are presented. Among others, the PDFs for the measures $h(l)$ and $m(l)$ are of central importance, and these quantities are studied in further detail in Section 4. Our previous theory on the multi-affinity of the X-field is reviewed

---

[a] e-mail: `nakao@ton.scphys.kyoto-u.ac.jp`

in Section 5, and some theoretical attempts are made in Section 6 toward the understanding of multi-fractality of the Y-field. Some discussions will be given in Section 7.

2 Models

In our previous studies [12,13], it was found that the type of turbulence of our present concern can generally arise in large assemblies of active dynamical elements when the following two conditions are satisfied:

1. The local (*i.e.*, temporally instantaneous) Lyapunov exponent defined for the individual element under forcing fluctuates irregularly between positive and negative values.
2. The driving field is stochastic and spatially nonuniform, but sufficiently long-waved so that any pair of nearby elements are driven similarly (but not identically).

Note that what are the specific origins of the drive and its stochasticity is not important. It may be generated internally, or given externally. In a special case, the strongly diffusive component in a certain reaction-diffusion system may take the role of such driving field provided the system is in a self-generated turbulent state [15].

We now propose the following model of randomly forced chaotic maps distributed on a one-dimensional lattice which is simple enough and can satisfy all the above requirements:

$$X_i(t+1) = (1-K)F(X_i(t)) + K\,G_i(t). \tag{1}$$

Here $F(z)$ represents the local map, $X_i(t)$ the amplitude of the ith element at time t, $G_i(t)$ the external field with strength parameter K. The prefactor $1-K$ before F is inserted to ensure that X_i is confined within a finite domain for the specific class of local maps considered below. The system length is fixed to 1 over which N elements are distributed, and the limit of large N will always be of our concern.

As for the local map $F(z)$, we choose two types of chaotic maps. The first one is given by an asymmetric tent map:

$$F(z) = \frac{z}{p} \quad (0 \le z \le p), \qquad \frac{1-z}{1-p} \quad (p \le z \le 1), \tag{2}$$

where p is a parameter controlling the peak position of the map. This map is composed of two linear parts of different slopes, so that its local Lyapunov exponent can fluctuate between two values, by which the first condition stated above is satisfied[1]. The corresponding model system (1) will be called model A.

The second model, which will be called model B, uses the standard logistic map for the local map:

$$F(z) = cz(1-z) \quad (0 \le z \le 1), \tag{3}$$

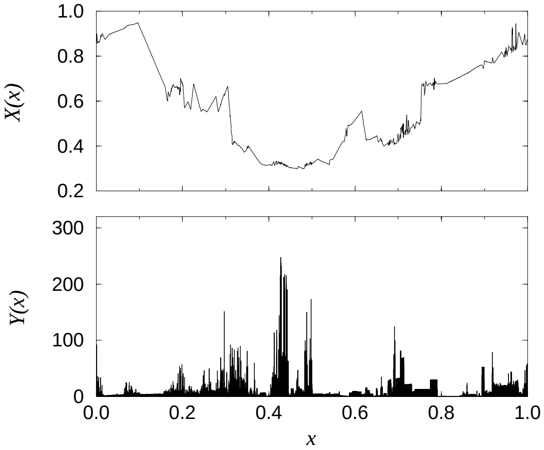

Fig. 1. Typical snapshot of the original X-field (top) and the corresponding difference Y-field (bottom) for model A. The scales of the axes follow the definitions given in Section 3.

where c is a bifurcation parameter. We already studied this model in our previous paper [13], and discovered singular behavior with multi-scaling properties.

Although the multi-scaling behavior itself turns out independent of the precise form of $F(z)$ as far as the fluctuation of the local Lyapunov exponent is allowed, the above simple choice for $F(z)$, especially model A, facilitates the analysis considerably. Except for a few minor points, scaling properties will be found qualitatively the same between the above two models, so that in what follows we will sometimes omit showing the data for model B unless the results differ significantly from model A.

Commonly to models A and B, the long-wave fluctuating external field $G_i(t)$ is assumed to be of the form:

$$G_i(t) = \frac{1}{2}\left[1 + \sin 2\pi\left(\frac{i + j(t)}{N}\right)\right], \tag{4}$$

where $j(t)$ is an integer chosen randomly from the interval $[0, N-1]$ at each time step. It is clear that the external force changes its phase (but not the amplitude) randomly, and it acts only on the Fourier component of the longest wavelength present in the system. Again, the precise form of $G_i(t)$ is irrelevant; as far as it is long-waved and randomly fluctuating, multi-scaling properties can be observed.

In the following numerical simulations, the parameter values are set $p = 0.75$ and $K = 0.45$ for model A, and $c = 3.7$ and $K = 2.2$ for model B. Thus, the height of the asymmetric tent map is given by $1 - K = 0.45$, and the effective bifurcation parameter of the logistic map is given by $(1-K)c = 2.885$. With these parameter values, each type of map is slightly below the threshold of chaotic transition. We have checked that multi-scaling properties can be seen in a wide range of parameters, and are by no means peculiar to the parameter values chosen above.

A typical snapshot of the amplitude field $X_i(t)$ for model A is illustrated at the top of Figure 1. The pattern looks intermittent in the sense that two distinctive

---

[1] Note that the smaller exponent can be negative, since the effective height of the map is multiplied by $1-K$.

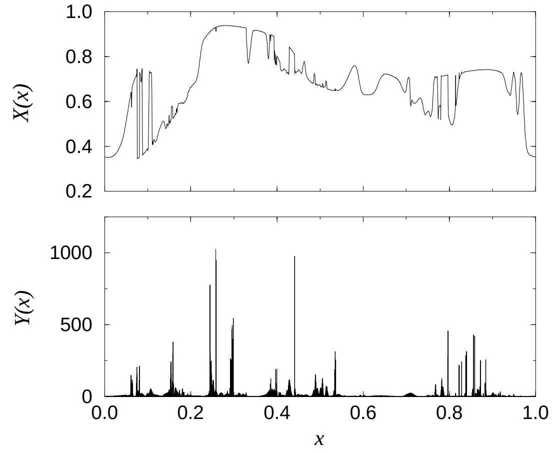

Fig. 2. Typical snapshot of the original X-field (top) and the corresponding difference Y-field (bottom) for model B.

parts coexist; in one part the spatial variation of the amplitude is smooth, while it is fluctuating violently in the other part presumably as a result of repeated foldings. At the bottom of Figure 1, the corresponding Y-field, defined here by $Y_i(t) := N|X_{i+1}(t) - X_i(t)|$, is displayed where the intermittency looks even stronger. Similar intermittent patterns are also seen for model B, which are given in Figure 2.

How to characterize these intermittent patterns and what is the mechanism for their appearance are the main concern of the present paper. We notice the strong resemblance of such patterns to those of the velocity and energy dissipation fields of homogeneous isotropic turbulence, and this resemblance motivates us to their multi-fractal analysis developed below.

3 Multi-scaling

We employ a multi-fractal formulation to characterize the intermittency of the X- and Y-fields. The multi-fractal concept has in fact turned out useful in characterizing singular measures in many physical systems such as fluid turbulence [1,2,7], chaotic attractors [8–10] and fractal growth patterns [3–6,16].

3.1 Preliminaries

Before proceeding, we define two types of measures which seem appropriate for characterizing each of the X- and Y-fields. In terms of these measures, we also give some definitions associated with the multi-fractal formulation.

Hereafter, we denote the lattice spacing as $\delta := 1/N$, and specify the position of the element as $x := i\delta$. We define the difference field $Y(x)$ as

$$Y(x) := \frac{X(x+\delta) - X(x)}{\delta} \,. \tag{5}$$

If $X(x)$ represents a smooth pattern, $Y(x)$ will approach the derivative $\mathrm{d}X(x)/\mathrm{d}x$ as $\delta \to 0$. The existence of this limit would not always be guaranteed, however, so we will retain δ to be finite though sufficiently small.

We now introduce two types of measures for the X- and Y-fields in a different way:

1. For the X-field, the measure $h(x,l)$ over the interval of length l around x is defined as

$$h(x,l) := |X(x+\frac{l}{2}) - X(x-\frac{l}{2})| \left(\simeq |\int_{x-\frac{l}{2}}^{x+\frac{l}{2}} Y(x')\mathrm{d}x'| \right). \tag{6}$$

   Namely, $h(l)$ gives an amplitude increment between two sites separated by a distance l.
2. For the Y-field, the measure $m(x,l)$ over the interval of length l around x is defined as

$$m(x,l) := \sum_{j=-\frac{l}{2\delta}}^{\frac{l}{2\delta}-1} |Y(x+j\delta)|\delta \left(\simeq \int_{x-\frac{l}{2}}^{x+\frac{l}{2}} |Y(x')|\mathrm{d}x' \right). \tag{7}$$

   Thus, $m(l)$ is given by the area formed by the $Y(x)$ curve over the interval of length l.

In what follows, our main concern will be the statistical properties of $h(l)$ and $m(l)$ for l sufficiently smaller than the system size, *i.e.*, $l \ll 1$.

The measure $h(l)$ is analogous to the velocity difference in fluid turbulence or the hight difference in fractal surface growth. On the other hand, $m(l)$ gives an analogue of the rate of energy dissipation integrated over a box of size l in fluid turbulence. Unlike the case of fluid turbulence, however, we used in the definition of Y the absolute value of the derivative of the original field X rather than its squared value, but this is simply a matter of convenience.

In terms of these measures, the multi-fractal formulation proceeds as follows. Our arguments developed for $h(l)$ and $m(l)$ are almost in parallel, except for slight differences in definition and terminology which are due to historical reasons.

First, the partition functions are defined as

$$Z_h^q(l) := \langle h(l)^q \rangle \simeq \left\langle \frac{1}{N(l)} \sum_{j=0}^{N(l)-1} h(x_j,l)^q \right\rangle ,$$

$$Z_m^q(l) := N(l)\langle m(l)^q \rangle \simeq \left\langle \sum_{j=0}^{N(l)-1} m(x_j,l)^q \right\rangle , \tag{8}$$

where $\langle \cdots \rangle$ stands for a statistical average; $N(l)$ is the number of boxes of size l, *i.e.*, $N(l) = l^{-1}$, and $x_j = (j + \frac{1}{2})l$ is the position of the jth box. Our results, especially the exponents for higher moments of the Y-field, depend on how the statistical average is taken. We will come back to this point later.

Borrowing the terminology from fully-developed turbulence, the partition function $Z_h^q(l)$ may be called *structure function* [2,17], while in fractal surface growth the corresponding quantity is called *height-height correlation* [3–6]. Note that $Z_h^q(l)$ for $q = 2$ is directly related to the short-range spatial correlation $\langle X(x)X(x+l)\rangle$, *i.e.*, the quantity we studied previously for some non-locally coupled systems [13]. On the other hand, the partition function $Z_m^q(l)$ is related to the correlation in the steepness of the original field X.

If the X- and Y-fields are multi-scaled, the corresponding partition functions are expected to scale as

$$Z_h^q(l) \sim l^{\zeta(q)}, \quad Z_m^q(l) \sim l^{\tau(q)}, \tag{9}$$

with q-dependent scaling exponents $\zeta(q)$ and $\tau(q)$. $\tau(q)$ is related to the generalized dimension $D(q)$ through $\tau(q) = (q-1)D(q)$. If the q-dependence of the exponents $\zeta(q)$ and $\tau(q)$ is nonlinear, the corresponding fields X and Y are called *multi-affine* and *multi-fractal*, respectively. Following the standard multi-fractal formulation, we assume that the local measures scale with l as

$$h(x,l) \sim l^{\beta(x)}, \quad m(x,l) \sim l^{\alpha(x)}, \tag{10}$$

and also that the numbers of boxes of size l needed to cover the sets with local scaling exponents β and α behave as

$$N_\beta(l) \sim l^{-g(\beta)}, \quad N_\alpha(l) \sim l^{-f(\alpha)}. \tag{11}$$

Since $g(\beta)$ and $f(\alpha)$ give the fractal dimensions of such sets, these functions are called dimension spectrums.

With these quantities, the partition functions are now expressed as

$$\begin{aligned} Z_h^q(l) &\sim N(l)^{-1} \int \mathrm{d}\beta l^{-g(\beta)} l^{\beta q} \sim l^{\beta^*(q)q - g(\beta^*(q))+1}, \\ Z_m^q(l) &\sim \int \mathrm{d}\alpha l^{-f(\alpha)} l^{\alpha q} \sim l^{\alpha^*(q)q - f(\alpha^*(q))}. \end{aligned} \tag{12}$$

Here the steepest descent method has been used, and $\beta^*(q)$ and $\alpha^*(q)$ are the values of α and β which minimize the exponents $\beta q - g(\beta) + 1$ and $\alpha q - f(\alpha)$, respectively. Thus, the scaling exponents $\zeta(q)$ and $\tau(q)$ are related to $g(\beta)$ and $f(\alpha)$ through the Legendre transforms:

$$\begin{aligned} \zeta(q) &= \min_\beta[\beta q - g(\beta) + 1], \ \tau(q) = \min_\alpha[\alpha q - f(\alpha)], \\ g(\beta) &= \min_q[\beta q - \zeta(q) + 1], \ f(\alpha) = \min_q[\alpha q - \tau(q)]. \end{aligned} \tag{13}$$

3.2 Numerical results

We now apply the multi-fractal analysis to our numerical data. The numerical calculation was carried out with the system size $N = 2^{14} \sim 2^{15}$ which seems large enough for the limiting behavior as $N \to \infty$ to be well inferred. The results obtained are qualitatively the same between models A and B.

We first investigate the multi-affinity of the original X-field. In Figure 3, numerically obtained partition functions $Z_h^q(l) = \langle h(l)^q \rangle$ for model A are plotted against l in log-log scales for several q values. Each curve clearly shows a power-law dependence for small l with the exponent $\zeta(q)$ increasing with q. Similar results are obtained for model B.

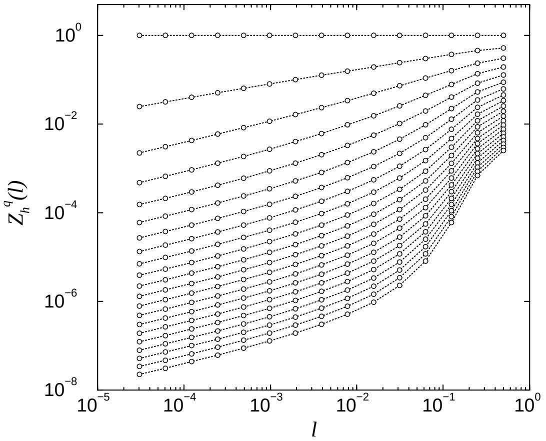

Fig. 3. Partition functions $Z_h^q(l)$ *vs.* l for model A. The data lying on a horizontal line corresponds to $q = 0$ and those on the line at the bottom to $q = 10$. The step of calculation is 0.5.

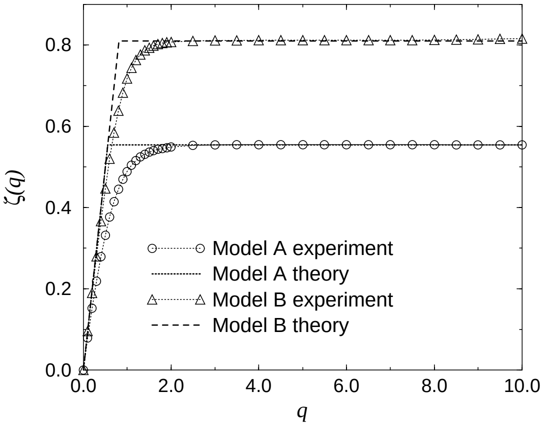

Fig. 4. Comparison of numerically obtained exponents $\zeta(q)$ *vs.* q with theoretical ones. The results are shown for models A and B.

Figure 4 shows the q-dependence of the exponents $\zeta(q)$ for models A and B, together with the theoretical curves predicted from our previous theory [12–14], *i.e.*,

$$\zeta(q) = q \ \ (0 < q < \eta), \quad \eta \ \ (\eta < q), \tag{14}$$

where η is a positive constant. According to our theory, the above expression is exact in the small l limit. Numerically obtained $\zeta(q)$ increases linearly with q in the small q region, and saturates to some constant for large q. Thus, $\zeta(q)$ is strongly nonlinear, or should rather be called "bi-linear" as a function of q, which gives clear evidence for the multi-affine nature of the original X-field in either of models A and B. Except for a slight discrepancy seen near the crossover region, the theoretical curves well reproduce

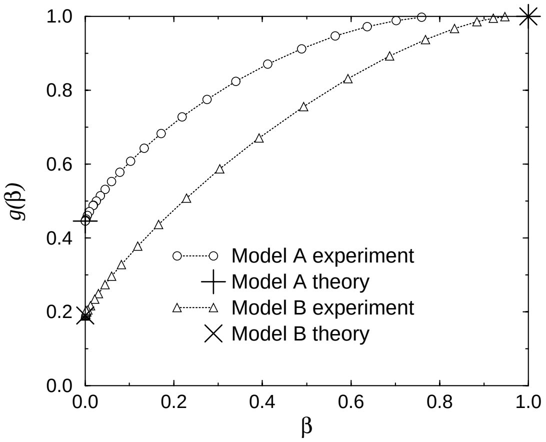

Fig. 5. Dimension spectrums $g(\beta)$ obtained numerically and theoretically for models A and B.

the numerical results[2]. For more accurate estimation of the exponent $\zeta(q)$, one may use the data for even smaller l simply by increasing N. This actually makes the bilinear behavior of $\zeta(q)$ even clearer, so we expect that a sharp transition from linear to constant behavior of $\zeta(q)$ will occur in the large N limit, precisely as predicted by the theory. This type of bilinear behavior of the exponent is also known for the velocity field of randomly forced Burgers equation, and called "bi-fractality" [2]. More generally, such a discontinuity in the q-derivative of the exponent is called "q-phase transition". Invariant measures of some chaotic attractors are known to exhibit q-phase transitions [9,10].

Figure 5 shows the resulting dimension spectrum $g(\beta)$. Theoretically, $g(\beta)$ consists of only two points corresponding to the two slopes of the $\zeta(q)$ curve, one of which lying on the $g(\beta)$-axis represents a singular component of the field, while the other point ($\beta = 1$, $g(\beta) = 1$) corresponds to smooth spatial variations of the field. The numerical $g(\beta)$ curve is inevitably continuous due to the aforementioned continuous change in the slope of the $\zeta(q)$ curve.

We now investigate the multi-fractality of the difference field Y. In Figure 6, numerically calculated partition functions $Z_m^q(l) = N(l)\langle m(l)^q \rangle$ *vs.* l for model A are shown in log-log scales. Various numerical curves corresponding to different q values obey power laws for small l, and their exponents increase with q. The scaling regime seems to be slightly broader than that for the X-field. Similar results are also obtained for model B.

The exponents $\tau(q)$ for various q are plotted in Figure 7. The resulting numerical curves show less remarkable bending as compared with the $\zeta(q)$ curves. Still their q-dependence is strongly nonlinear, indicating the multi-fractality of the Y-field. Each curve identically satisfies $\tau(0) = -1$ and $\tau(1) = 0$, *i.e.*, the conditions demanded by the facts that the measure is space-filling and that the total measure $l^{-1}\langle m(l) \rangle$ is a constant independent of l. The curves seem to be asymptotically linear for large q.

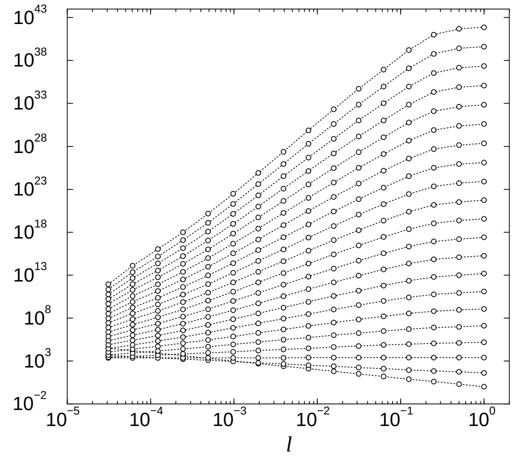

Fig. 6. Partition functions $Z_m^q(l)$ *vs.* l for model A, where q is changed from 10 (top) to 0 (bottom) with a step of 0.5.

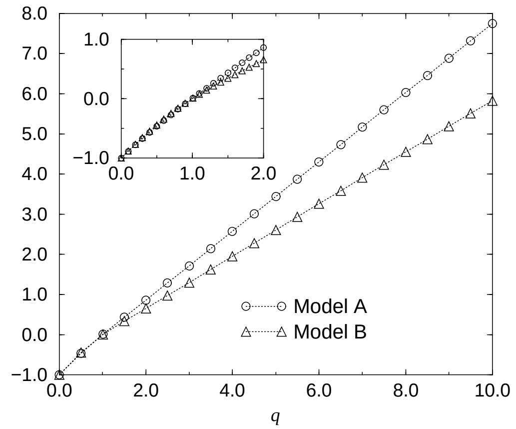

Fig. 7. Exponents $\tau(q)$ for models A and B. The inset is a blowup of the small q region.

The generalized dimension $D(q)$ is shown in Figure 8. In each model, the $D(q)$ curve seems to decrease linearly with q for small q. Note that the log-normal theory predicts such linearity. On the other hand, corresponding to the asymptotic linearity of the function $\tau(q)$, each $D(q)$ curve should saturate to a constant for large q. Our numerical results even suggest that in the limit of large N, $D(q)$ becomes constant, *i.e.*, $D(q) = D(\infty)$, above a certain q_c, while it remains linear below q_c, implying a sharp transition at q_c. Actually, as we let δ decrease by increasing N, and look into the region of smaller l, the transition of $D(q)$ between linear and constant behaviors seems to become sharper.

Figure 9 shows the dimension spectrum $f(\alpha)$. As expected, the spectrum is given by a convex function of α and tangent to the line $f(\alpha) = \alpha$. It is also tangent to $f(\alpha) = 1$ at its extremum, which comes from the fact that the metric support of the Y-field is identical

---

[2] In reference [13], this theoretical expression was confirmed numerically for the logistic maps. For the present case of asymmetric tent maps (model A) as well as logistic maps (model B), the value of η is estimated from the asymptotic behavior of $\zeta(q)$ for large q. This value will be identified with the slope of the PDF later in the present paper.

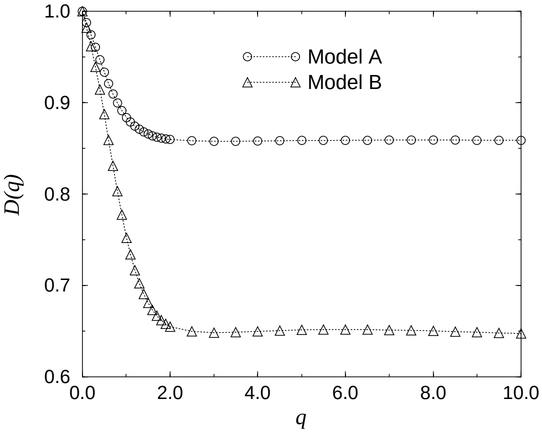

Fig. 8. Generalized dimensions $D(q)$ for models A and B.

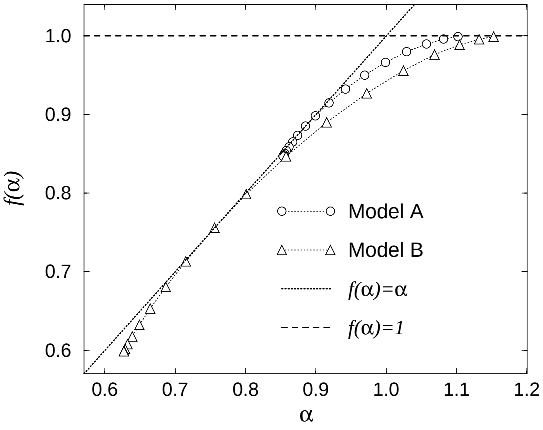

Fig. 9. Dimension spectrums $f(\alpha)$ for models A and B.

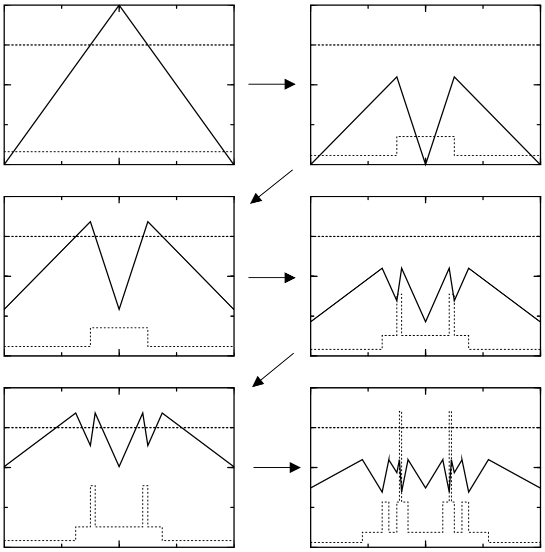

Fig. 10. Schematic evolution of the X- (solid line) and Y- (dotted line) field for model A. The evolution from one time step to the next can be decomposed into two elementary processes, *i.e.*, the application of the map (indicated by a horizontal arrow) and the application of the external drive (indicated by an oblique arrow).

with the embedding space. Corresponding to the above-mentioned sharp transition in the $D(q)$ curve, the $f(\alpha)$ curve has a left endpoint at $\alpha = D(\infty)$; singularities smaller than this value do not seem to exist.

We have thus demonstrated the multi-affinity and multi-fractality of the X- and Y-fields, respectively. Note that the calculated $\zeta(q)$ and $\tau(q)$ are only for positive q, thus giving only the left half of the $g(\beta)$ and $f(\alpha)$ curves. Moments for negative q, which are not only difficult to obtain, seems also non-universal and hence less important; they are associated with very small differences of the original field X depending on the details of the model such as the specific functional form of the external field.

3.3 Origin of multi-scaling

We have seen that a simple assembly of maps can exhibit nontrivial multi-scaling behavior. Its origin should be explored now. On an intuitive level, this may look rather easy to understand if we keep watching the evolution of the field patterns for a while. Take model A (asymmetric tent maps) for simplicity. With the parameter values assumed before, each individual map is not chaotic and has a stable fixed point. Consequently, if the forcing is not applied, the elements will soon fall into the fixed point, and both the X- and Y-fields will become spatially uniform. In the presence of randomly fluctuating long-wave external field, in contrast, a certain fraction of the elements which are kicked off the fixed point will exhibit chaotic transients before falling into the fixed point. This means that stretching-and-folding of the field pattern persists locally for some time, and this will lead to fractalized or intermittent amplitude patterns. Still the patterns, however violent their spatial variation may look, will maintain their continuity as far as the local Lyapunov exponent of the individual element remains negative on average. This is because the elements are all synchronous with the external drive, implying mutual synchrony between any neighboring pair of elements with infinitesimal spacing. The resulting pattern may look like something between smooth and scattered patterns.

Figure 10 explains schematically the above-described process for model A. The figure shows the evolution of the X- and Y-fields over several time steps, and we expect such a process should be observed typically at small spatial scales. It is assumed here that the external field is almost uniform over a sufficiently small region, so that its only effect is to give a uniform shift to the values of X, thus having no direct effect on the Y-field. We can see that the X- and Y-fields evolve step by step into increasingly complex patterns similar to what is observed in numerical simulations.

The evolution of our system from one time step to the next can be decomposed into two consecutive operations on each small part of the system. The first operation is the local map. If a small segment of the pattern stays above the line $X(x) = p$, this operation will stretch it and then fold it, while the part below this p-line will simply be compressed. The other operation is the action of the external field. The X-value of each element is shifted by an amount proportional to the amplitude of the external filed, and the latter is varying from place to place. The amounts of the shift experienced by elements sitting closely are nearly the same but not identical, because the external field is long-waved. The combination of this strongly correlated forcing and the effect of occasional local instabilities produces peculiar spatial correlations among the elements with small mutual distances. It is interesting to compare such dynamics of the X-field to the simple multi-affine cascade model introduced by Benzi *et al.* [18].

The evolution of the Y-field corresponding to the X-field is superimposed in the same figure. Since Y is given by a (coarse-grained) derivative of the X-field, the evolution of local Y is governed by its successive multiplication by the two random numbers corresponding to the two slopes of the asymmetric tent map. As the original X-field fractalizes, the intervals over which a common multiplier is applied becomes smaller and smaller, and this leads to the intermittent pattern of the Y-field. Such a process may be viewed as a random multiplicative cascade similar to the weighted curdling model, and is thus expected to produce multi-fractal measures.

For model B (logistic maps), the dynamics is a little more complicated, because the local Lyapunov exponents take continuous values. Still we expect that the underlying mechanisms producing multi-affine and multi-fractal measures would be essentially the same as for model A, and that they are again given by random multiplicative cascade processes. The next problem is how to describe such processes on a more quantitative level.

4 Probability distribution functions of the measures

In order to study quantitatively the random multiplicative processes underlying the multi-scaling, we introduce probability distribution functions (PDFs) $P(h;l)$ and $Q(m;l)$ respectively for the measures $h(l)$ and $m(l)$. It is also convenient to introduce rescaled measures $\bar{h}(l) = h(l)/l$ and $\bar{m}(l) = m(l)/l$, and corresponding rescaled PDFs $\bar{P}(\bar{h};l) = (\mathrm{d}h/\mathrm{d}\bar{h})P(h;l)$ and $\bar{Q}(\bar{m};l) = (\mathrm{d}m/\mathrm{d}\bar{m})Q(m;l)$. With these PDFs, the partition functions are expressed as

$$\begin{aligned} Z_h^q(l) &= \langle h(l)^q \rangle = \int_0^\infty h^q P(h;l)\mathrm{d}h \\ &= l^q \int_0^\infty \bar{h}^q \bar{P}(\bar{h};l)\mathrm{d}\bar{h} = l^q \langle \bar{h}(l)^q \rangle, \\ Z_m^q(l) &= N(l)\langle m(l)^q \rangle = N(l) \int_0^\infty m^q Q(m;l)\mathrm{d}m \\ &= l^{q-1} \int_0^\infty \bar{m}^q \bar{Q}(\bar{m};l)\mathrm{d}\bar{m} = l^{q-1}\langle \bar{m}(l)^q \rangle. \end{aligned} \quad (15)$$

Multi-scaling properties can completely be specified by these PDFs.

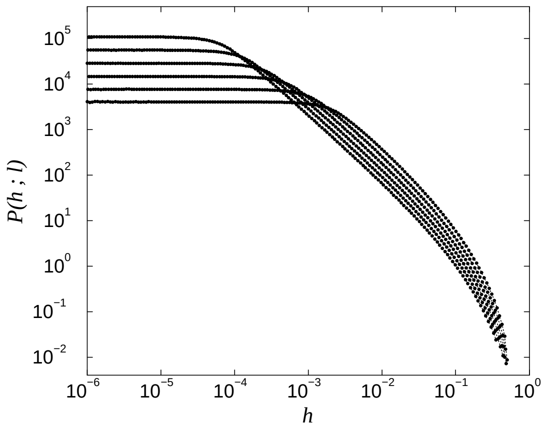

Fig. 11. PDF of the height difference $h(l)$ for model A. The curves correspond to $l = 2^{-15}$ (highest level of saturation at lower h), 2^{-14}, 2^{-13}, 2^{-12}, 2^{-11}, and 2^{-10} (lowest).

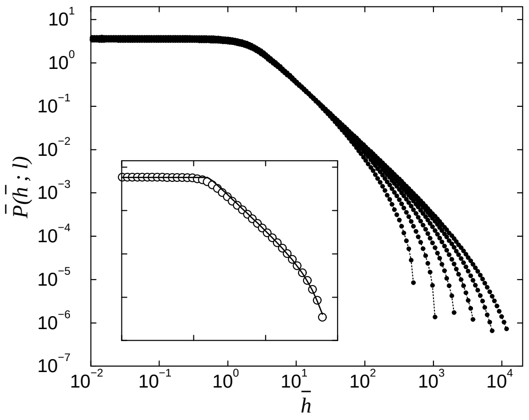

Fig. 12. PDF of the rescaled height difference $\bar{h}(l)$ for model A, where $l = 2^{-15}$ (slowest decay), 2^{-14}, 2^{-13}, 2^{-12}, 2^{-11}, and 2^{-10} (fastest decay). Fitting by a power law multiplied by an exponential for the case of $l = 2^{-13}$ with $\eta = 0.55$ and $\bar{h}_0 = 1150$ is shown in the inset.

Let us examine the PDF for the X-field first. Figure 11 shows $P(h;l)$ with different l obtained numerically for model A. They are apparently non-Gaussian, reflecting the strong spatial intermittency of the X-field. Each PDF curve remains almost constant up to some h (lower cutoff), above which exhibiting a power-law decay, and starting to drop suddenly around some h (higher cutoff). The area of flat PDF apparently extends with l, while the exponent of the power-law decay and the higher cutoff position seem almost invariant. The corresponding rescaled PDFs $\bar{P}(\bar{h};l)$ are shown in Figure 12. The higher cutoff now moves to the left with l, but otherwise the rescaled PDF, especially the lower cutoff, seems almost invariant. Looking into the decaying part of the rescaled PDF more carefully, we find that the numerical data are well fitted by a power law multiplied by an exponential:

$$\bar{P}(\bar{h};l) \sim \bar{h}^{-1-\eta} \exp\left(-\frac{\bar{h}}{\bar{h}_0(l)}\right) \quad (\bar{h} \gg 1). \quad (16)$$

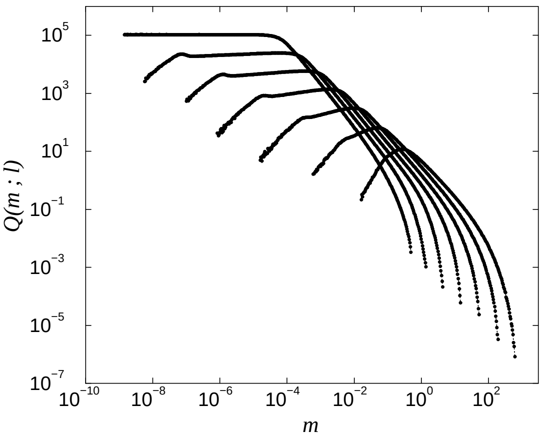

Fig. 13. PDF of the area $m(l)$ for model A, where $l = 2^{-15}$, 2^{-13}, 2^{-11}, 2^{-9}, 2^{-7}, 2^{-5}, and 2^{-3}. The peak of PDF drifts to the right with the increase of l.

Here η is a positive constant, and $\bar{h}_0(l)$ is a l-dependent positive parameter which determines the higher cutoff. The above empirical form is compared with the actual PDF for $l = 2^{-13}$ in the inset of Figure 12. It will turn out later that the exponent η is identical with the quantity in equation (14) under the same notation. η is determined from the statistics of the local Lyapunov exponent, and, as stated before, the X-field maintains a spatial continuity as far as $\eta > 0$. It is obvious that $\bar{h}_0(l) \propto l^{-1}$, since we rescaled the original cutoff position by l^{-1}. This means that the power-law scaling regime of $\bar{P}(\bar{h};l)$ will become indefinitely extended as l tends to zero. This fact is relevant to the q-phase transition of $\zeta(q)$, as we see later. The results for model B are found to be qualitatively the same as for model A.

Let us now examine the PDF for the Y-field. In Figure 13, $Q(m;l)$ for different values of l are shown. They may look similar to $P(h;l)$. Actually, they are more or less flat up to some value of the measure m, exhibiting power-law decay in the intermediate region, and dropping quickly beyond a certain cutoff. Again, the lower cutoff shifts to the right with l, and the exponent of the power-law decay is independent of l. However, there are a few important differences between $Q(m;l)$ and $P(h;l)$. First, $Q(m;l)$ is not really flat below the lower cutoff; $Q(m;l)$ for each $l > \delta$ starts to decay below some m. Furthermore, the higher cutoff now depends on l. Figure 14 shows the corresponding rescaled PDFs $\bar{Q}(\bar{m};l)$. The lower cutoff then becomes almost constant, and the higher cutoff moves to the left with l. Note, however, that the l-dependence here is much weaker than that for $\bar{P}(\bar{h};l)$.

In contrast to the case of the X-field, the small $\bar{m}$ behavior of the rescaled PDF depends more strongly on l. It would be interesting to compare such behavior of $\bar{Q}(\bar{m};l)$ with log-normal distribution, and this will be done later. It is remarkable that, as shown in the inset of Figure 14 and also in Figure 15, the large $\bar{m}$ behavior of the rescaled PDF (the power-law decaying part and the higher cutoff) is well fitted by an inverse power of $\bar{m}$ multiplied by a stretched exponential function[3]:

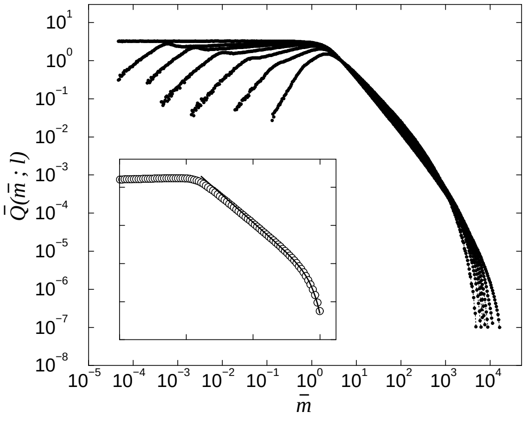

Fig. 14. PDF of the rescaled area $\bar{m}(l)$ for model A, where $l = 2^{-15}$, 2^{-13}, 2^{-11}, 2^{-9}, 2^{-7}, 2^{-5}, and 2^{-3}. See Figure 13 for identification of the curves. Fitting by a power law multiplied by a stretched exponential to the PDF for $l = 2^{-11}$ with $\eta = 0.55$, $\bar{m}_0 = 4280$, and $\gamma = 1.6$ is shown in the inset.

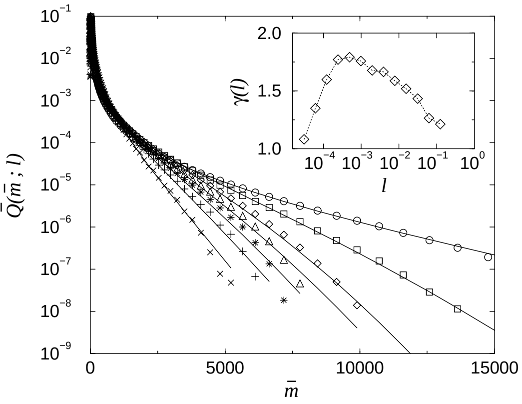

Fig. 15. Linear-log plot of the tail of rescaled PDF for model A. The data are shown for $l = 2^{-15}$, 2^{-13}, 2^{-11}, 2^{-9}, 2^{-7}, 2^{-5}, and 2^{-3} with increasing steepness of the curves in this order. The solid lines indicate stretched-exponential fits to the data. Estimated exponents $\gamma(l)$ of the tail are plotted in the inset.

$$\bar{Q}(\bar{m};l) \sim \bar{m}^{-1-\eta} \exp\left[-\left(\frac{\bar{m}}{\bar{m}_0(l)}\right)^{\gamma(l)}\right] \qquad (\bar{m} \gg 1), \tag{17}$$

where η is a positive constant, and $\bar{m}_0(l)$ and $\gamma(l)$ are l-dependent parameters. Note that the above η can be identified with the quantity η appearing in equation (16), because $\bar{h}(\delta) \equiv \bar{m}(\delta)$ and $\bar{P}(\bar{h};\delta) \equiv \bar{Q}(\bar{m};\delta)$ by definition.

While the cutoff $\bar{h}_0(l)$ was seen to be simply proportional to l^{-1}, this is not the case for $\bar{m}_0(l)$. Indeed, as shown in Figure 16 where $\bar{m}_0(l)$ *vs.* l is plotted in log-log scales, we have a nontrivial power law $\bar{m}_0(l) \propto l^{-\nu}$

---

[3] Precisely speaking, it is actually not a stretched but a 'squeezed' exponential because $\gamma(l) > 1$.

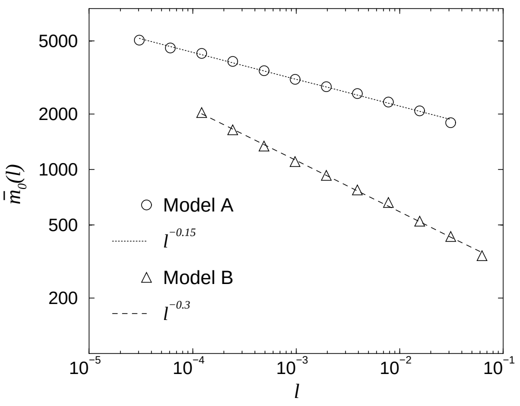

Fig. 16. Log-log plot of the cutoff $\bar{m}_0(l)$ of the tail *vs.* l. Results for models A and B are shown.

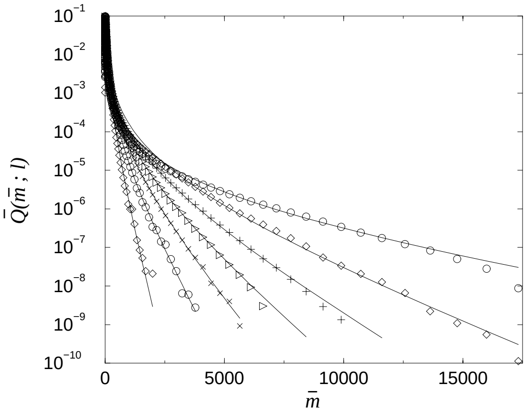

Fig. 17. Linear-log plot of the tail of the rescaled PDF for model B. The data are shown for $l = 2^{-15}$, 2^{-13}, 2^{-11}, 2^{-9}, 2^{-7}, 2^{-5}, and 2^{-3} with increasing steepness of the curves in this order. The solid lines indicate exponential fits to the data.

with $\nu \simeq 0.15$. As we see later, ν is an important exponent characterizing the intermittency. The inset of Figure 15 shows the exponents $\gamma(l)$ *vs.* l in log-linear scales. They depend weakly on l, but stay between 1 and 2. We confirmed that these results, especially the value of ν and hence the cutoff $\bar{m}_0(l)$, are virtually independent of N for large N.

The PDF $Q(m;l)$ for model B is found roughly the same as for model A. The only difference to be noticed is that, as is seen from Figure 17, the tail of the PDF for model B is better fitted with a power law multiplied by a simple exponential rather than a stretched exponential. Thus, $\gamma(l)$ may be fixed to 1 in equation (17) for model B. As shown in Figure 16, the cutoff $\bar{m}_0(l)$ for model B also exhibits power-law dependence on l like $\bar{m}_0(l) \sim l^{-\nu}$ with $\nu \simeq 0.3$.

This property of the cutoff $\bar{m}_0(l)$ means that, as in the case of $\bar{P}(\bar{h};l)$, the power-law scaling regime of $\bar{Q}(\bar{m};l)$ extends indefinitely as l goes to zero. As we see later, this fact is responsible for a sharp transition of the $D(q)$ curve.

5 Theory of the multi-affinity of the X-field

In our previous studies [12–14], we developed a PDF-based theory which successfully explained the multi-affinity of the X-field and the origin of the related exponent $\zeta(q)$. We first give its brief review, but with a slight modification so that some detailed features of our numerical results may better be captured. An explanation for the exponent $\tau(q)$ of the multi-fractal Y-field will be attempted in the next section.

5.1 Calculation of the scaling exponent from the PDF

We observed in the preceding section that the rescaled PDF $\bar{P}(\bar{h};l)$ may be approximated in the following form:

$$\bar{P}(\bar{h};l) = \begin{cases} \bar{P}_0(l) & (0 < \bar{h} < 1), \\ \bar{P}_1(l)\bar{h}^{-1-\eta}\exp\left(-\dfrac{\bar{h}}{\bar{h}_0(l)}\right) & (1 < \bar{h}). \end{cases} \tag{18}$$

In the above, the rescaled variables are used so that the transition from constant behavior to power-law behavior may always occur at $\bar{h} = 1$. As before, we have $\bar{h}_0(l) \propto l^{-1}$. The l-dependent constants $\bar{P}_0(l)$ and $\bar{P}_1(l)$ are determined from the conditions of normalization and continuity of the PDF.

Using the above approximate form of the PDF, we obtain

$$\langle \bar{h}(l)^q \rangle = \frac{\dfrac{1}{1+q} + \bar{h}_0(l)^{q-\eta}\Gamma\left(q-\eta, \dfrac{1}{\bar{h}_0(l)}\right)\exp\left(\dfrac{1}{\bar{h}_0(l)}\right)}{1+\bar{h}_0(l)^{-\eta}\Gamma\left(-\eta, \dfrac{1}{\bar{h}_0(l)}\right)\exp\left(\dfrac{1}{\bar{h}_0(l)}\right)}, \tag{19}$$

where $\Gamma(z,p)$ is an incomplete gamma function defined by $\Gamma(z,p) := \int_p^\infty \mathrm{e}^{-t}t^{z-1}\mathrm{d}t$.

For sufficiently small l, equation (19) can be simplified drastically. By noting that $\frac{1}{\bar{h}_0(l)}$ is $O(l)$, the gamma function and the exponential function may be regarded as l-independent. Therefore, the l-dependence of $\langle \bar{h}(l)^q \rangle$ comes essentially from the terms $\bar{h}_0(l)^{q-\eta}$ and $\bar{h}_0(l)^{-\eta}$, so that we obtain

$$\langle \bar{h}(l)^q \rangle \simeq \frac{a_q + b_q l^{\eta-q}}{a_0 + b_0 l^\eta} \simeq \frac{a_q}{a_0} + \frac{b_q}{a_0} l^{\eta-q}, \tag{20}$$

where a_q and b_q are q-dependent constants. Thus,

$$\langle \bar{h}(l)^q \rangle \simeq \frac{a_q}{a_0} \;\; (\eta - q > 0), \qquad \frac{b_q}{a_0} l^{\eta-q} \;\; (\eta - q < 0), \tag{21}$$

and the partition function $Z_h^q(l) = l^q \langle \bar{h}(l)^q \rangle$ is expressed as

$$Z_h^q(l) \simeq \frac{a_q}{a_0}\, l^q \;\; (\eta - q > 0), \qquad \frac{b_q}{a_0}\, l^\eta \;\; (\eta - q < 0). \tag{22}$$

We are thus led to a scaling form:

$$Z_h^q(l) \sim l^{\zeta(q)}, \tag{23}$$

with the bi-fractal exponent:

$$\zeta(q) = q \ \ (0 < q < \eta), \quad \eta \ \ (\eta < q). \tag{24}$$

In this way, the multi-affine exponent $\zeta(q)$ is determined from the exponent η of the power-law decay of the PDF. Actually, for model A, we obtain $\eta \simeq 0.55$ from our data of the PDF in Figure 12, and this value coincides roughly with the asymptotic value of $\zeta(q)$ for large q (see Fig. 4). Such consistency can also be confirmed for model B.

The bi-fractality of $\zeta(q)$ could only be revealed for extremely small l, by which the power-law tail of the PDF becomes sufficiently extended. Of course, such a property presupposes that our system has no minimal characteristic length scale.

5.2 Microscopic model for the PDF

It is also possible to give a microscopic explanation of the observed shape of the PDF such as given by equation (18). This can be achieved by considering the dynamics of the height difference $h(l)$.

Let us denote the height difference without the absolute sign as $h(t;l)$, which is now regarded as a dynamical variable and can take both positive and negative values. It is easily understood [12–14] that $h(t;l)$ for small l is driven multiplicatively by a chaotic motion of the individual element and also subjected to an additive noise. The strength of the additive noise is proportional to l, because its source is the amplitude difference of the long-wave driving field between the two sites separated by a distance l. We adopt a continuous-time and linear approximations. Then, $h(t;l)$ obeys the following multiplicative stochastic equation[4,5]:

$$\frac{\mathrm{d}h(t;l)}{\mathrm{d}t} = \lambda(t)\ h(t;l) + l\ \xi(t). \tag{25}$$

The statistics of the random factors $\lambda(t)$ and $\xi(t)$ are relevant to the stationary PDF obtained from the above equation. However, statistical property of $\lambda(t)$, which is identical with the local statistics of the Lyapunov exponent associated with an element, will not be trivial. Thus, in what follows, we work with a simplifying assumption that $\lambda(t)$ are Gaussian-white noises. The same properties are also assumed for $\xi(t)$. We denote the mean and the variance of the multiplicative noise $\lambda(t)$ as λ_0 and D_λ, respectively. The mean of the additive noise $l\xi(t)$ is 0 due to symmetry. The standard deviation of $l\xi(t)$, which specifies the boundary between the constant behavior and the power-law behavior of the stationary PDF, is $O(l)$. Thus, for the purpose of qualitative argument, one may simply assume that the transition occurs at $|h| = l$. We further assume reflective boundary conditions at $|h| = 1$ in order to incorporate the effects of nonlinear damping which is absent in equation (25). The PDF $P(h;l)$ is obtained as a stationary solution of the Fokker-Planck equation corresponding to equation (25). Although one can calculate it explicitly under the conditions described above, the following approximate form would be sufficient for the present purpose:

$$P(h;l) = \begin{cases} P_0 & (0 < h < l), \\ P_1 h^{-1-\eta} & (l < h < 1), \\ 0 & (1 < h). \end{cases} \tag{26}$$

Here we again consider only the case of $h > 0$, because $P(h;l)$ is apparently symmetric with regard to $h = 0$. η is determined from the statistics of the multiplicative noise and is given by $\eta = \lambda_0/D_\lambda$ [12–14]. By rescaling, equation (26) reduces to

$$\bar{P}(\bar{h};l) = \begin{cases} \bar{P}_0 & (0 < \bar{h} < 1), \\ \bar{P}_1 \bar{h}^{-1-\eta} & (1 < \bar{h} < l^{-1}), \\ 0 & (l^{-1} < \bar{h}). \end{cases} \tag{27}$$

The above result is qualitatively the same as equation (18), by which we mean that our PDF is composed of two distinct parts; in one of which is constant while in the other exhibits power-law decay with a cutoff at $\bar{h} \propto l^{-1}$. Indeed, any moments calculated from this simplified PDF gives identical results with the case of the exponential damping, equation (14) [14].

The exponential damping of the tail of the PDF assumed in equation (18), which represents the observed results more quantitatively, will be obtained by including a nonlinear term explicitly in equation (25) instead of the reflective wall as[6].

$$\frac{\mathrm{d}h(t;l)}{\mathrm{d}t} = \lambda(t)\ h(t;l) - h(t;l)^2 + l\ \xi(t). \tag{28}$$

We have thus succeeded in a "microscopic" explanation of the multi-affinity of the X-field on the basis of some moderate approximations and simplifying assumptions. It should be emphasized that the statistics of the local Lyapunov exponent is relevant to the specific form of multi-affinity. For more detailed calculations, see reference [14].

6 On the multi-fractality of the Y-field

The remaining problem is to explain the exponent $\tau(q)$ of the multi-fractal Y-field. It seems, however, that the shape

---

[4] One may consider a discrete time model as well, but the results will remain unchanged as far as the scaling exponents of the moments are concerned [13].

[5] This equation is nothing but the multiplicative Langevin equation frequently used to describe the noisy on-off intermittency [14]. Indeed, we can observe that the height differences between nearby elements exhibit noisy on-off intermittency in our numerical simulation.

[6] Since our argument is only qualitative, we ignored a constant factor which should in practice come before the nonlinear term here.

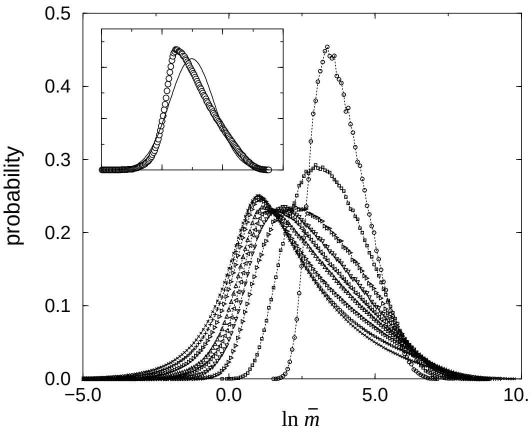

Fig. 18. PDF of $\ln\bar{m}$ for model A, where $l = 2^{-15}$, 2^{-10}, 2^{-7}, 2^{-5}, 2^{-4}, 2^{-3}, 2^{-2}, 2^{-1}, and 1. The peak drifts to the right with the increase of l. A log-normal fit to the PDF for $l = 2^{-5}$ is shown in the inset.

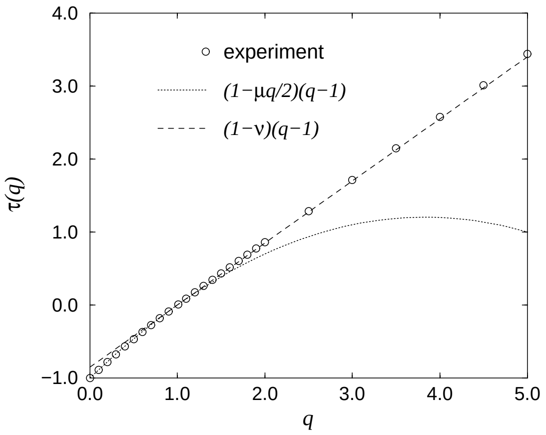

Fig. 19. Exponent $\tau(q)$ for model A; experiment *vs.* theory.

of the PDF is not so simple as that for the X-field, and could not be approximated so easily. It also seems difficult to give a microscopic explanation for it.

Therefore, we first try to extract the exponent from the experimental PDF approximately in two asymptotic regimes. As already shown, our PDF has a power-law decay part of the form $\bar{m}^{-1-\eta}$ in the middle. For the sake of convenience, let us call the three distinct regimes of the PDF I, II, and III from the left. Then, the above statement implies that some lower moments whose order q is less than η will be governed by regime I of the PDF, while the moments with q higher that η will be governed by regime III or a boundary area between II and III. Thus, we expect that the transition point $q_{\rm c}$ of the $D(q)$ curve is close to η, which was also the case for $\zeta(q)$. Furthermore, as we mentioned before, the central power-law regime (regime II) can be extended indefinitely by letting l go to zero. This makes the transition between the above-mentioned two asymptotic regimes, and hence the transition of $D(q)$ across $q \simeq q_{\rm c}$ sharper and sharper.

In what follows, we see why a microscopic description of the underlying mechanism is not so easy. This leads us to the study of multiplier distributions. Actually, the multiplier distribution characterizes the cascade process through scales, and its analysis could be a first step toward the understanding of the underlying microscopic mechanism.

6.1 Log-normal approximation of the PDF for lower moments

We have seen that the lower moments of $\bar{m}(l)$ are dominated by regime I. Since $\bar{Q}(\bar{m};l)$ can not be regarded as constant in this regime, however, their estimation would not be so simple. Being motivated by the observed linear behavior of the $D(q)$ curve for small q, which is consistent with the log-normal theory, we examine to what extent the log-normal model can be applied to our system. Figure 18, which concerns model A, shows how the PDF as a function of $\ln\bar{m}$ develops with the scale l. We find that, as l becomes smaller, the width of the PDF becomes wider and its peak drifts to the left, reflecting the intermittent nature of the Y-field. If such a PDF is approximated by some simple analytic function, then one may calculate the scaling exponent of the moments explicitly. For doing this, we should note that $l^{-1}\langle m(l)\rangle \equiv \langle\bar{m}(l)\rangle$ is independent of l because the total measure is invariant. As a simplest approximation, we represent our PDF with a log-normal distribution with its first and second moments identical with the observed ones.

A log-normal distribution is expressed as

$$\bar{Q}(\bar{m};l) = \frac{1}{\sqrt{2\pi v(l)}\,\bar{m}} \exp\left[-\frac{(\ln\bar{m} - c(l))^2}{2v(l)}\right], \qquad (29)$$

where $c(l)$ and $v(l)$ are the mean and the variance of $\ln\bar{m}$. It is further assumed that $c(l)$ and $v(l)$ take the form:

$$c(l) = \ln\langle\bar{m}(l)\rangle + \frac{\mu}{2}\ln l, \quad v(l) = -\mu\ln l, \qquad (30)$$

where μ gives the so-called intermittency exponent. The condition that $\langle\bar{m}(l)\rangle$ must not depend on l is automatically satisfied with the above $c(l)$ and $v(l)$.

The qth moment of $\bar{m}(l)$ is calculated as

$$\langle\bar{m}(l)^q\rangle = \langle\bar{m}(l)\rangle^q l^{-\frac{\mu}{2}q(q-1)}, \qquad (31)$$

and the partition function is expressed as

$$Z_m^q(l) = N(l)\langle m(l)^q\rangle = \langle\bar{m}(l)\rangle^q l^{q-1-\frac{\mu}{2}q(q-1)}. \qquad (32)$$

Thus, the exponent $\tau(q)$ and the generalized dimension $D(q)$ are obtained as

$$\tau(q) = (1 - \frac{\mu}{2}q)(q-1), \quad D(q) = 1 - \frac{\mu}{2}q. \qquad (33)$$

In Figure 19, which also concerns model A, numerically obtained $\tau(q)$ is compared with the formula in equation (33) for $\tau(q)$ with $\mu = 0.3$, showing a good agreement for $q < 2$. Thus, the log-normal model may seem to work well for lower moments.

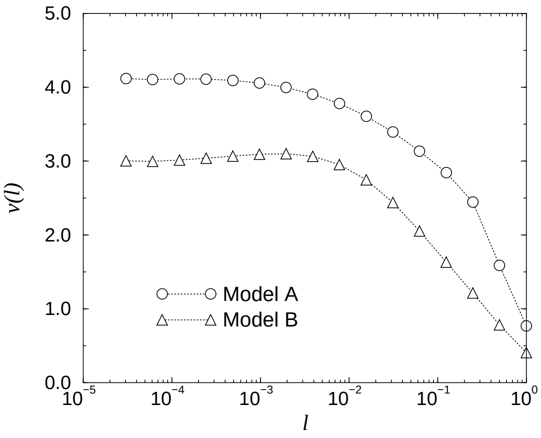

Fig. 20. Variance $v(l)$ of the PDF of $\ln \bar{m}$ for models A and B.

However, the log-normal PDF looks considerably different from the actual PDF, and the assumed forms for $c(l)$ and $v(l)$ in equation (30) do not seem to hold. The inset of Figure 18 shows a typical log-normal fit to $\bar{Q}(\bar{m};l)$ for $l = 2^{-5}$. We used there the observed values of mean and variance. It is clear that the actual PDF is asymmetric and deviates considerably from the log-normal PDF. The fitting parameter $v(l)$ *vs.* l is plotted in Figure 20. If the assumptions in equation (30) were correct, then the data should lie on a straight line with its slope identical to the intermittency exponent μ. Although our $v(l)$ is a decreasing function of $\ln l$, it is by no means linear and it is difficult to read out a slope in a sensible way.

The PDF $\bar{Q}(\bar{m};l)$ for model B is more or less symmetric for larger l, so that log-normality seems to hold better. One may read out from Figure 20 a mean gradient of $v(l)$ as $\mu \sim 0.6$, and this roughly gives the value ~ 0.3 of the slope of the $D(q)$ curve for small q values (see Fig. 8). As l becomes even smaller, the asymmetry of the PDF $\bar{Q}(\bar{m};l)$ becomes stronger and the log-normal approximation becomes worse again.

For small l, the changes of $c(l)$ and $v(l)$ seem so small that the observed scaling behavior comes primarily from the increasing asymmetry of the PDF rather than from the l-dependence of $c(l)$ and $v(l)$. Therefore, the symmetric log-normal distribution is not a good approximation to the observed PDF at small scales, and the formula (33) for the exponents can not be justified from the experimental PDF.

6.2 Stretched exponential tails of the PDF and higher moments

Higher moments are governed by the tail (regimes II and III) of the PDF. We have seen that our PDF is well fitted by a power law multiplied by a stretched exponential (or by a simple exponential for model B). The power-law dependence of the cutoff $\bar{m}_0(l)$ on l leads naturally to the linear dependence of $\tau(q)$ on q.

According to our previous observation, we can assume the rescaled PDF $\bar{Q}(\bar{m};l)$ to take the approximate form:

$$\bar{Q}(\bar{m};l) = \begin{cases} \bar{Q}_0(\bar{m};l) & (\bar{m} < 1), \\ \bar{Q}_1(l)\bar{m}^{-1-\eta} \exp\left[-\left(\dfrac{\bar{m}}{\bar{m}_0(l)}\right)^{\gamma(l)}\right] & (\bar{m} > 1), \end{cases} \tag{34}$$

where $\bar{Q}_0(\bar{m};l)$ is an unknown function of $\bar{m}$ representing the small $\bar{m}$ behavior of the PDF, and $\bar{Q}_1(l)$ is a constant yet to be fixed. The l-dependence of these quantities must satisfy the normalization and continuity conditions. We rescaled $\bar{m}$ again so that the two distinct regimes of the PDF are matched at $\bar{m} = 1$.

With the above PDF, the qth moment $\langle \bar{m}(l)^q \rangle$ is calculated as

$$\langle \bar{m}(l)^q \rangle = \frac{\int_0^1 \bar{m}^q \bar{Q}_0(\bar{m};l)\mathrm{d}\bar{m} + \bar{Q}_1(l)\frac{1}{\gamma(l)}\bar{m}_0(l)^{q-\eta}\Gamma\left(\frac{q-\eta}{\gamma(l)}, \frac{1}{\bar{m}_0(l)^{\gamma(l)}}\right)}{\int_0^1 \bar{Q}_0(\bar{m};l)\mathrm{d}\bar{m} + \bar{Q}_1(l)\frac{1}{\gamma(l)}\bar{m}_0(l)^{-\eta}\Gamma\left(\frac{-\eta}{\gamma(l)}, \frac{1}{\bar{m}_0(l)^{\gamma(l)}}\right)}. \tag{35}$$

The asymptotic behavior of $\langle \bar{m}(l)^q \rangle$ for small l is governed by a power law, and in order to find its exponent, we may use the fact that the observed $\bar{m}_0(l)$ behaves like $\bar{m}_0(l) \propto l^{-\nu}$ with some positive ν. Under the conditions $q \gg q_\mathrm{c} \simeq \eta > 0$ and $l \ll 1$, $\bar{m}_0(l)$ is very large and the gamma functions become nearly independent of l. Therefore, the second term in the numerator and the first term in the denominator will dominate (note that we are treating the case of $\eta > 0$). Neglecting the other terms, we obtain

$$\begin{aligned} \langle \bar{m}(l)^q \rangle &\sim \frac{\bar{Q}_1(l)\frac{1}{\gamma(l)}\Gamma\left(\frac{q-\eta}{\gamma(l)}, \frac{1}{\bar{m}_0(l)^{\gamma(l)}}\right)}{\int_0^1 \bar{Q}_0(\bar{m};l)\mathrm{d}\bar{m}}\,\bar{m}_0(l)^{q-\eta} \\ &\sim u(l)\, l^{-\nu(q-\eta)}, \end{aligned} \tag{36}$$

where $u(l)$ is an unknown function of l but related to the other unknowns $\bar{Q}_0(\bar{m};l)$ and $\bar{Q}_1(l)$ in a certain way. The partition function $Z_m^q(l)$ is calculated as

$$\begin{aligned} Z_m^q(l) &= N(l)\langle m(l)^q \rangle = l^{q-1}\,\langle \bar{m}(l)^q \rangle \\ &\sim u(l) l^{q-1-\nu(q-\eta)}. \end{aligned} \tag{37}$$

The entire form of $\tau(q)$ cannot be determined because the function $u(l)$ is unknown. Still the q-dependence of $\tau(q)$ can be obtained as

$$\tau(q) = (1-\nu)q + \mathrm{const.}, \tag{38}$$

from which we obtain $D(\infty) = 1-\nu$. On the other hand, as shown in Figure 8, the observed $D(q)$ curve seems almost constant, *i.e.*, $D(q) \equiv D(\infty)$ for q larger than a certain $q_\mathrm{c} \simeq \eta$. This means that the above constant is close to $\nu - 1$, so that the equality

$$\tau(q) = (1-\nu)(q-1), \quad D(q) = 1-\nu \tag{39}$$

is conjectured for $q \gg q_c \simeq \eta$.

In Figure 19, which concerns model A, the above expression for $\tau(q)$ with $\nu \simeq 0.15$, *i.e.*, the value estimated from Figure 16, is compared with the observed $\tau(q)$. As expected, the data for $\tau(q)$ are fitted nicely for $q > 2$. We can also confirm the validity of this result from Figure 8 where the saturated value of $D(q)$ is roughly given by $1 - \nu \simeq 0.85$. For model B, the saturated value $\simeq 0.65$ of $D(q)$ is consistent with the previously obtained value $\nu \simeq 0.3$.

Thus, the linear q-dependence of the higher exponents comes from the power-law dependence of the cutoff position $\bar{m}_0(l)$ of the (stretched-)exponential tail on l. Similar arguments relating the stretched-exponential tail to the linearity of $\tau(q)$ curve can be found in reference [19].

6.3 Difficulty in developing a microscopic model for the PDF

From our success in developing a theory for the PDF $P(h;l)$, one may expect that a similar microscopic theory could be developed for explaining the shape of $Q(m;l)$. We suspect that $Q(m;l)$ might be obtained as a stationary solution to some simple stochastic equation similar to equation (28) for $P(h;l)$.

Let us work with the rescaled variable $\bar{m}(l)$. The large $\bar{m}$ behavior of the PDF given by equation (17) seems easier to explain. In fact, inverse power of $\bar{m}$ multiplied by a stretched exponential can be obtained as a stationary distribution of the Fokker-Planck equation equivalent to the following multiplicative stochastic equation with nonlinear damping:

$$\frac{\mathrm{d}\bar{m}(t;l)}{\mathrm{d}t} = \lambda(t)\ \bar{m}(t;l) - A(l)\ \bar{m}(t;l)^{p(l)}. \tag{40}$$

Here $A(l)$ and $p(l)$ are assumed l-dependent, and they determine where the boundaries between distinct regimes of the PDF are placed, and also determine the exponent of the stretched exponential function. The multiplicative noise $\lambda(t)$ is assumed to be of the same nature as before. Instead of introducing an additive noise as we did in equation (28) to represent the fluctuations of the applied external field, let us substitute the same effect by imposing a reflective boundary condition at $\bar{m} = 1$. The stationary PDF can then be obtained as

$$\bar{Q}(\bar{m};l) \propto \bar{m}^{-1-\eta} \exp\left(-\frac{A(l)\bar{m}^{p(l)-1}}{D_\lambda\,(p(l)-1)}\right), \tag{41}$$

which is in fact the form we expected.

The stochastic equation (40), especially the nonlinear damping $\bar{m}(t;l)^{p(l)}$ and its coefficient $A(l)$ responsible for the scaling behavior of $Z_m^q(l)$, does not seem to be justified so easily as for the nonlinear term $h(t;l)^2$ in equation (28). The term $A(l)\bar{m}(t;l)^{p(l)}$, together with an additional *ad hoc* assumption $A(l) \propto l^\nu$ (which is necessary to explain the observed $\tau(q)$ curve), could be imagined as representing some averaged effects of the microscopic dynamics.

The above-mentioned difficulty of explaining the Y-field dynamics comes from the fact that the measure $\bar{m}(l)$ (or $m(l)$) is a quantity which involves the spatial correlations of height differences in some intricate way. The local Lyapunov exponents of nearby elements are strongly correlated, but they are not identical. Consequently, the elements in a local group within scale l may behave synchronously for some time but may occasionally lose synchrony and exhibit independent behavior. The power-law decay of $\bar{Q}(\bar{m};l)$ with $\bar{m}$ may be viewed as a result of the linear multiplicative process of $\bar{m}(l)$ with common multipliers, which produces a coherent motion of the elements, while the sudden drop of $\bar{Q}(\bar{m};l)$ for larger $\bar{m}$ which is crucial to the scaling behavior, seems to occur as a result of some subtle correlation in the local Lyapunov exponents among the elements. The small $\bar{m}$ behavior of the PDF, which is not simply constant, seems also difficult to explain.

Thus, we are yet unable to give a plausible argument justifying the assumed stochastic equation for $m(l)$ to the same level as for $h(l)$. Since spatial correlation in the local Lyapunov exponents seems to be crucial, we now convert to a different picture which seems to incorporate such correlation in a more natural way.

6.4 Multiplier distributions

As an alternative approach to the Y-field dynamics, we try to characterize the spatial intermittency of the field in terms of a binary cascade model with a scale-invariant multiplier distribution [20–25]. As we mentioned before, the real cascade process in our model is complicated. The length and the position of each interval where the same multiplier is applied vary from time to time.

Here we adopt a conservative binary cascade model which seems to be the simplest way for capturing the peculiar spatial correlation of the local Lyapunov exponents. We numerically calculate the multipliers, and examine to what extent this cascade model is applicable to our system. In the binary cascade model, the measure on a interval is subdivided into two measures on two subintervals of equal length. The subdivision of the measure is done by a random multiplier p picked up independently from a certain scale-independent distribution $R(p)$. $R(p)$ is assumed to be symmetric with regard to $p = 0.5$, *i.e.*, $R(1-p) = R(p)$.

The exponent $\tau(q)$ and $R(p)$ are related as follows [2]. We assume the total measure to be normalized to 1. At the nth step of the cascade, the length of each interval becomes $l = 1/2^n$, and the measure $m(l)$ on it is given by $m(l) = p_1 p_2 ... p_n$, where p_is are random multipliers picked up independently from $R(p)$. The qth moment of $m(l)$ is calculated as $\langle m(l)^q \rangle = \langle (p_1 p_2 ... p_n)^q \rangle = \langle p^q \rangle^n$, where $\langle \cdots \rangle$ stands for the ensemble average with regard to $R(p)$. Thus, the partition function $Z_m^q(l)$ is expressed as

$$Z_m^q(l) = N(l)\langle m(l)^q \rangle = l^{-1}\langle p^q \rangle^n \sim l^{\tau(q)}, \tag{42}$$

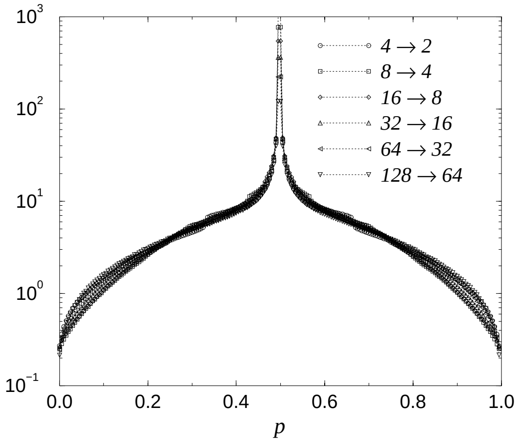

Fig. 21. Linear-log plot of the multiplier distribution $R(p)$ *vs.* p for model A.

and $\tau(q)$ is given by

$$\tau(q) = \frac{\ln\left(l^{-1}\langle p^q\rangle^n\right)}{\ln l} = \frac{n\ln\langle p^q\rangle}{\ln\left(1/2^n\right)} - 1 = -\frac{\ln\langle p^q\rangle}{\ln 2} - 1. \tag{43}$$

We now try to find an actual multiplier distribution $R(p)$ from numerical data using $N = 2^{15}$ elements. We calculated $R(p)$ for various n, and this is shown in Figure 21 for model A. Each $R(p)$ has a peak at $p = 0.5$, and seems to collapse on a single scale-invariant curve. $R(p)$s for scales larger than $2^8(\times 2^{-15})$ do not collapse on this curve. In Figure 22, the right half of the distribution $R(p)$ *vs.* $p-0.5$ ($p > 0.5$) is shown in log-log scales. The approximate scale-invariant curve seems to obey a power law for small $p-0.5$, while it decays quickly for larger $p-0.5$. As indicated in the same figure, this curve can be well fitted by a power law multiplied by a stretched exponential.

However, as shown in Figure 23, the corresponding $\tau(q)$ calculated from the empirically postulated $R(p)$ cannot reproduce the actual $\tau(q)$ obtained previously except for lower moments. This implies that the fluctuation of the total measure or the strong correlation of $R(p)$s between scales, which are both ignored in the above model, are important. The slight discrepancy in the tail of $R(p)$s between different scales may also be important. Such difficulties arising in the multiplier description are already pointed out in the context of fluid turbulence [22–24].

Furthermore, as shown in Figure 24, the multiplier distributions for model B are not scale-invariant at all. Each distribution has its peak at $p = 0.5$ again, but the distribution narrows with decreasing l with no sign of collapse on a single scale-invariant curve.

7 Discussion

7.1 Schemes of averaging

As we mentioned previously, our results depend on the averaging method. We discuss here the way in which statistical averages are taken in our numerical calculations.

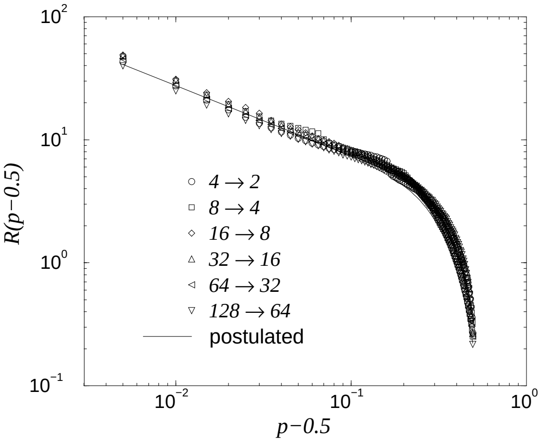

Fig. 22. Log-log plot of the multiplier distribution $R(p-0.5)$ *vs.* $p-0.5$ for model A. Fitting by a power law multiplied by a stretched exponential, *i.e.*, $R(p-0.5) \propto (p-0.5)^{-0.57} \exp\left\{-\left[(p-0.5)/0.36\right]^{3.0}\right\}$, is also shown.

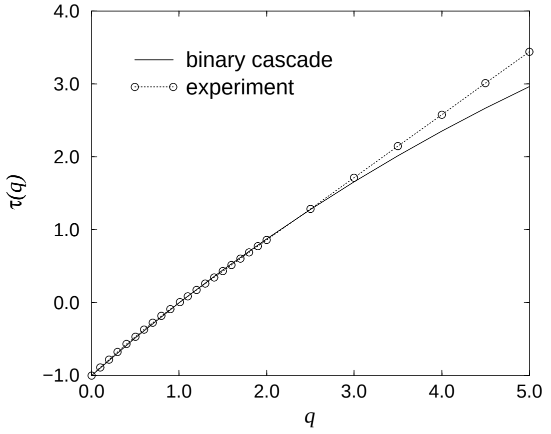

Fig. 23. Numerically obtained exponent $\tau(q)$ and that estimated from a binary cascade model with the postulated multiplier distribution $R(p)$.

What we actually did is a simple space-time average. Namely, we first sum up $h(x,l)^q$ or $m(x,l)^q$ over the entire system at a given instant and then over a long time-sequence, and finally divide it by a suitable factor to obtain the average. Halsey [16] called this type of average annealed average, because this amounts to calculate the exponent from equation (9) with the use of $\ln\langle \hat{Z}^q_{h,m}(l)\rangle$, where $\hat{Z}^q_{h,m}(l)$ are the partition functions calculated at each time step. This type of average is used, for example, in analyzing long-time experimental data obtained from turbulent flows [7].

Now, we touch upon other types of averages and their results briefly. In the so-called quenched average [16], we estimate the exponent from formula (9) with the use of $\langle \ln \hat{Z}^q_{h,m}(l)\rangle$. This means that we calculate the logarithm of the spatial sum of the moments at each time step, and then take the average over time. Multi-fractal analysis of DLA clusters sometimes uses this scheme.

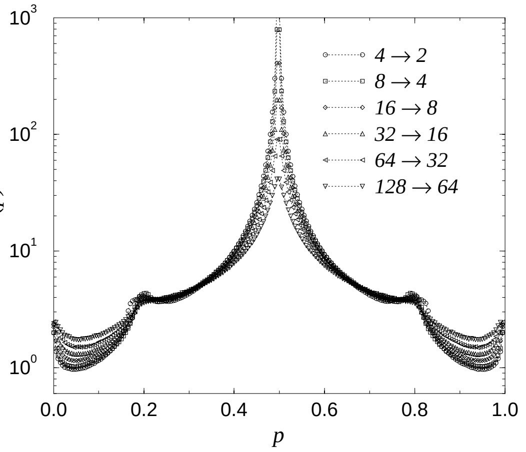

Fig. 24. Linear-log plot of the multiplier distribution $R(p)$ *vs.* p for model B.

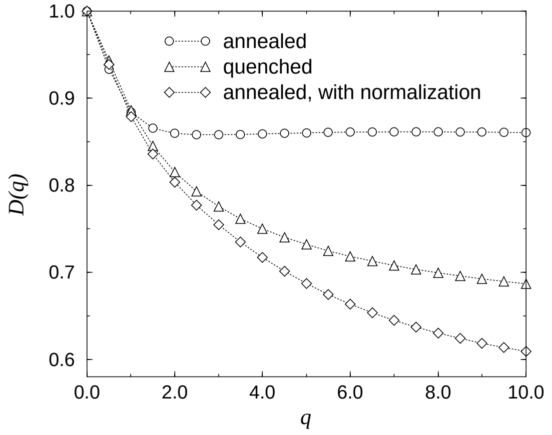

Fig. 25. Generalized dimensions $D(q)$ for model A calculated with three different schemes of averaging.

We used yet another scheme of averaging in our previous paper [13]. It is similar to the annealed average, but the difference is that we normalize the measure at each time step. This amounts to ignoring the temporal fluctuations of the total measure.

In the first scheme of averaging, we are regarding the whole spatio-temporal sequence of the measure as one large sample. The other schemes of averaging treat the measure at each time step to be one sample, and take an ensemble average over the samples. The latter two schemes have a tendency to ignore the fluctuation of the total measure. This indeed makes a great difference, because the fluctuation of the total measure in our systems does not obey the central limit theorem, and diverges in the $N \to \infty$ limit.

Figure 25 shows the generalized dimensions $D(q)$ for model A calculated with the above three different schemes of averaging. Interestingly, the exponents obtained with the use of the last two schemes exhibit rather smooth change with q, with no indication of a sharp transition. Thus, the fluctuation of the total measure seems crucial to the observed q-phase transition. The $D(q)$ curves obtained by the latter two methods may reflect some other kinds of scale-invariance hold in different asymptotic regimes from the first one.

7.2 Similarity and dissimilarity to fluid turbulence

We studied the multi-scaling properties observed in systems of chaotic elements subjected to long-wave random external forcing. In spite of its simplicity, our model shows typical multi-scaling properties, *i.e.*, multi-affinity of the amplitude field and multi-fractality of its coarse-grained spatial derivative.

Although we emphasized the similarity of our model to fluid turbulence, there are a number of important differences, some of which are the following. In our system there is no such property as postulated by Kolmogorov's refined similarity hypothesis which is crucial to the understanding of fully-developed turbulence. This seems to be due to the absence of conservation laws in our system, and as a result, the scaling properties observed in the amplitude field and those in its spatial derivative are difficult to interrelate in a simple way. For the same reason, in trying to find a coherent picture for various scaling properties observed in our system, the problem cannot be boiled down to the problem of a single field dynamics, while in the fully developed turbulence there are good reasons to believe that all nontrivial scaling properties observed come basically from the dynamics of the energy dissipation field.

Our model has no intrinsic minimal length scale, so that the scaling regime has no lower cutoff length. This seems to give the reason for the occurrence of q-phase transition in our system. If we introduce a minimal characteristic length scale, *e.g.*, by assuming diffusive coupling between nearest neighbor pairs of elements, then no clear q-phase transition could be observed.

7.3 Toward the explanation of the multi-fractality of the Y-field

The multi-affinity of the original amplitude field was rather easy to explain, and we could develop a theory which consistently explains the scaling properties. The characteristic shape of the PDF generated by simple multiplicative stochastic processes recently attracted considerable attention in connection with on-off intermittency, economical model, and self-organized criticality. See references [14,26,27] and references therein.

The multi-fractality of the Y-field was not so easy to explain, however. We could only develop a crude phenomenological model which enables to estimate the values of the exponents from the data for the PDF in two asymptotic regimes. Specifically, we applied the log-normal approximation for the lower moments. It fits the numerical data well but not completely. Further study will clarify the source of the discrepancy. Note that, also in fully-developed turbulence, the log-normal model is nothing more than a crude approximation to the experimentally observed PDF [17].

The exponents for the higher moments were explained from our numerical finding that the tail of the PDF fits nicely with a simple functional form, *i.e.*, a power law multiplied by a stretched exponential, with a cutoff parameter given by some power of l. Stretched exponential tails are frequently observed in many systems such as fluid turbulence [2,28,29], fractal surface growth [5], and economy [30]. The appearance of the same functional form in our system implies the existence of some dynamical processes of common nature going on in these systems. Studies in this direction can be found, for example, in reference [31].

In the log-normal approximation of the small $\bar{m}$ behavior of the PDF, we introduced a phenomenological parameter μ. On the other hand, in the stretched-exponential approximation of the tail of the PDF, we found another phenomenological parameter ν. Each represents the effect of intermittency, but without their clearer physical interpretation yet.

The binary cascade model we used in this paper works with discrete spatial scales with a single multiplier distribution. There also exists more sophisticated cascade models based on continuous scales for turbulent flow, which describes the evolution of the PDF with the scale by a Fokker-Planck equation [32], or by a Langevin equation with scale-dependent non-Gaussian noise [33]. It will also be interesting to apply such ideas to our system.

Finally, although we do not have a satisfactory theory of the observed characteristic shape of the $D(q)$ curve yet, it seems to be a generic property commonly shared by the type of turbulent state we studied, as in the case of the $\zeta(q)$ curve. For example, we found that qualitatively the same shape of the $D(q)$ curve is also observed in the spatio-temporal chaotic regime of non-locally coupled complex Ginzburg-Landau oscillators. Some kind of theory, which can quantitatively explain the spatial correlation of the fluctuation of the Y-field from the microscopic equation, should be developed in the future.

We are grateful to P. Marcq and H. Chaté for useful comments and advice. One of the author (H. N.) acknowledges the support by JSPS Research Fellowships for Young Scientists.

References

1. G. Parisi, U. Frisch, in *Turbulence and Predictability in Geophysical Fluid Dynamics and Climate Dynamics*, edited by M. Ghil, R. Benzi, G. Parisi (North-Holland, Amsterdam, 1985), p. 84.
2. U. Frisch, *Turbulence, the legacy of A.N. Kolmogorov* (Cambridge University Press, 1995).
3. A.-L. Barabási, T. Vicsek, Phys. Rev. A **44**, 2730 (1991).
4. A.-L. Barabási, H.E. Stanley, *Fractal Concepts in Surface Growth* (Cambridge University Press, 1995).
5. J. Krug, Phys. Rev. Lett. **72**, 2907 (1994).
6. C. Dasgupta, J.M. Kim, M. Dutta, S. Das Sarma, Phys. Rev. E **55**, 2235 (1997).
7. C. Meneveau, K.R. Sreenevasan, Nucl. Phys. B Proc. Suppl. **2**, 49 (1987); J. Fluid. Mech. **224**, 429 (1991).
8. T.C. Halsey, M.H. Jensen, L.P. Kadanoff, I. Procaccia, B.I. Shraiman, Phys. Rev. A **33**, 1141 (1986).
9. E. Ott, *Chaos in Dynamical Systems* (Cambridge University Press, 1993).
10. C. Beck, F. Schlögl, *Thermodynamics of Chaotic Systems* (Cambridge University Press, 1993).
11. Y. Kuramoto, H. Nakao, Physica D **103**, 294 (1997).
12. Y. Kuramoto, H. Nakao, Phys. Rev. Lett. **76**, 4352 (1996).
13. Y. Kuramoto, H. Nakao, Phys. Rev. Lett. **78**, 4039 (1997).
14. H. Nakao, Phys. Rev. E **58**, 1591 (1998).
15. Y. Kuramoto, D. Battogtokh, H. Nakao, Phys. Rev. Lett. **81**, 3543 (1998).
16. T.C. Halsey, K. Honda, B. Duplantier, J. Stat. Phys. **85**, 681 (1996).
17. A.S. Monin, A.M. Yaglom, *Statistical Fluid Mechanics, Vol. 2*, edited by J.L. Lumeley (MIT Press, Cambridge, Mass., 1975).
18. R. Benzi, L. Biferale, A. Crisanti, G. Paladin, M. Vergasolla, A. Vulpiani, Physica D **65**, 352 (1993).
19. A. Bershadskii, Physica A **234**, 611 (1997).
20. E.A. Novikov, Phys. Fluids A **2**, 814 (1990).
21. A.B. Chhabra, K.R. Sreenivasan, Phys. Rev. Lett. **68**, 2762 (1992).
22. K.R. Sreenivasan, G. Stolovitzky, J. Stat. Phys. **78**, 311 (1995).
23. G. Pedrizzetti, E.A. Novikov, A.A. Praskovsky, Phys. Rev. E **53**, 475 (1996).
24. M. Nelkin, G. Stolovitzky, Phys. Rev. E **54**, 5100 (1996).
25. I. Hosokawa, Proc. R. Soc. Lond. A **453**, 691 (1997).
26. H. Takayasu, A-H. Sato, M. Takayasu, Phys. Rev. Lett. **79**, 966 (1997).
27. D. Sornette, Physica A **250**, 295 (1998).
28. R. Benzi, L. Biferale, G. Paladin, A. Vulpiani, M. Vergassola, Phys. Rev. Lett. **67**, 2299 (1991).
29. P. Kailasnath, K.R. Sreenivasan, G. Stolovitzky, Phys. Rev. Lett. **68**, 2766 (1992).
30. J. Laherrère, D. Sornette, Eur. Phys. J. B **2**, 525 (1998).
31. U. Frisch, D. Sornette, J. Phys. I France **7**, 1155 (1997).
32. A. Naert, R. Friedrich, J. Peinke, Phys. Rev. E **56**, 6719 (1997); Phys. Rev. Lett. **78**, 863 (1997).
33. P. Marcq, A. Naert, Physica D **124**, 368 (1998).